EUROPEAN ORGANISATION FOR NUCLEAR RESEARCH (CERN)

Submitted to: JHEP

CERN-EP-2022-179
17th November 2022

Search for new phenomena in multi-body invariant masses in events with at least one isolated lepton and two jets using $\sqrt{s}$ = 13 TeV proton–proton collision data collected by the ATLAS detector

The ATLAS Collaboration

A search for resonances in events with at least one isolated lepton (e or μ) and two jets is performed using 139 fb^{-1} of $\sqrt{s}$ = 13 TeV proton–proton collision data recorded by the ATLAS detector at the LHC. Deviations from a smoothly falling background hypothesis are tested in three- and four-body invariant mass distributions constructed from leptons and jets, including jets identified as originating from bottom quarks. Model-independent limits on generic resonances characterised by cascade decays of particles leading to multiple jets and leptons in the final state are presented. The limits are calculated using Gaussian shapes with different widths for the invariant masses. The multi-body invariant masses are also used to set 95% confidence level upper limits on the cross-section times branching ratios for the production and subsequent decay of resonances predicted by several new physics scenarios.

1 Introduction

Searches for resonances in dijet invariant mass distributions provide a means to investigate a wide range of theories beyond the Standard Model (BSM theories). Such searches are sensitive to heavy particles that decay into two partons (quarks or gluons) which, following hadronisation, form jets (i.e. dijets). Previous searches for heavy resonances in dijet mass distributions performed by ATLAS [1–3] and CMS [4–6] have set limits on the production of heavy resonances over a range of masses for a variety of BSM models.

Searches in dijet mass distributions were also performed in events triggered by leptons [7]. In contrast to the searches in inclusive dijet events, an exclusive selection requiring events with a light lepton (electron e or muon μ, referred to simply as a 'lepton' herein) in addition to dijets in the final state increases the sensitivity to various exotic models. Using lepton triggers to select these events provides a means to study low-mass regions that are difficult to access in inclusive dijet events, where the large jet production rate imposes high threshold requirements on jet triggers. In addition, requiring an additional lepton reduces the QCD multi-jet background rate and thus can be favourable for BSM model searches. A recent ATLAS search [8] similarly looked for resonances in complementary final states with $Z \rightarrow ll + X$ events.

The searches [7] for a heavy dijet resonance in two-jet events triggered by leptons can be extended into a search for a resonance in a final state which includes two jets (jj) and a lepton (ℓ). Searches for narrow peaks in three-body decays (such as invariant masses of two jets and a lepton, $m_{jj\ell}$) are sensitive to a new class of models with cascade decays of heavy particles which have not been studied extensively at the LHC. Such studies in multi-body decays can be performed in exactly the same way as searches for resonances in dijet mass (m_{jj}) distributions using a data-driven technique for background determination [9]. This technique mitigates problems arising from insufficient theoretical knowledge of the Standard Model (SM) background in Monte Carlo (MC) simulations.

There are a number of theoretical models [10–15] that, for a certain choices of parameters, can exhibit resonance-like structures in multi-body invariant masses. For example [9], the invariant mass $m_{jj\ell}$ for decays such as $X \rightarrow Y\,W \rightarrow jj\ell\nu$ (with a W boson decaying to $\ell\nu$) can be used in searches for a heavy unknown particle X in scenarios where the mass-splitting between X and a second unknown particle Y is not large (a few hundred GeV). This leads to a relatively small transverse momentum for the neutrino. Therefore, the inclusion of missing transverse momentum may not improve the reconstruction of X masses.

More generally, a generic s-channel process, $X \rightarrow Y\,C$, can be considered, where X is an unknown heavy particle. The particles Y and C are SM or BSM particles that produce quarks, gluons, leptons or other particles via two-body decay kinematics. As a result, an enhancement in multi-body invariant masses is expected near the mass of the particle X, which can be used in searches. However, two-body invariant masses may not be the best tool for identifying such events if Y and C are broad resonances. The experimental limitations due to large widths, $\Gamma/m > 0.15$ (where Γ is the width and m is the mass of a resonance), of dijet resonances are discussed in the previous dijet searches [1–3, 7].

This study reports model-independent searches for new phenomena in three- and four-body invariant mass distributions in events with at least one isolated lepton. Such searches can lead to the discovery of heavy resonances with cascade decays in situations where two-body decays are broad, or affected by a large SM background. Three- and four-body masses have not been explored extensively at the LHC using data-driven techniques for background determination. These invariant masses are also used here to study a number of specific BSM models, such as dark-matter models with an axial-vector mediator [10], the Sequential Standard Model with W' and Z' bosons [11], composite resonances breaking lepton-flavour universality

[13], and radion models [14, 15]. The search uses an integrated luminosity of 139 fb^{-1} of $\sqrt{s}$ = 13 TeV proton–proton collision data recorded by the ATLAS detector.

2 ATLAS detector

The ATLAS detector [16–18] consists of an inner tracking detector (ID), surrounded by a superconducting solenoid which provides a 2 T magnetic field, electromagnetic and hadronic calorimeters, and a muon spectrometer (MS). The ID provides tracking in the pseudorapidity[1] region $|\eta| \leq 2.5$ and consists of silicon pixel and microstrip detectors surrounded by a transition radiation tracker, which also provides information for electron identification. Each tracking detector consists of a central barrel and two endcap sections.

The electromagnetic calorimeter is a sampling device made of lead absorbers with liquid argon (LAr) as active medium. It comprises a barrel ($|\eta| \leq 1.475$) and two endcaps ($1.375 \leq |\eta| \leq 3.2$). To facilitate corrections for energy losses upstream of the calorimeter, the cryostat is equipped with a presampler layer in the region $|\eta| \leq 1.8$. Hadronic sampling calorimetry is provided by a steel and scintillator-tile calorimeter in the region $|\eta| \leq 1.7$, complemented by a copper/LAr system in the region $1.5 \leq |\eta| \leq 3.2$. The forward region ($3.1 \leq |\eta| \leq 4.9$) is equipped with both electromagnetic and hadronic calorimeters composed of copper/LAr and tungsten/LAr, respectively.

The muon spectrometer is the outermost ATLAS subsystem. It detects muons in the pseudorapidity region up to $|\eta| = 2.7$, with triggering capability up to $|\eta| = 2.4$. The spectrometer consists of a barrel ($|\eta| \leq 1.05$) and two endcap sections ($1.05 \leq |\eta| \leq 2.7$). A system of three large superconducting air-core toroidal magnets, each with eight coils, provides a magnetic field with a bending integral of about 2.5 Tm in the barrel and up to 6 Tm in the endcaps.

The trigger system [19] consists of a first-level trigger implemented in hardware using a subset of the detector information to accept events from the 40 MHz bunch crossings at a rate of 100 kHz, followed by a software-based trigger implemented in a large computer farm, which reduces the acceptance rate so that events are recorded at about 1 kHz. An extensive software suite [20] is used in data simulation, in the reconstruction and analysis of real and simulated data, in detector operations, and in the trigger and data acquisition systems of the experiment.

3 Monte Carlo simulations

Monte Carlo (MC) simulations of various SM background processes are used to estimate their contributions to the multi-body mass distributions and to validate some aspects of the analysis procedure. The considered sources of SM background are the QCD multi-jet, $t\bar{t}$, single-top and W+jets processes. The QCD multi-jet event sample was created at leading order in QCD with parton showering using the Pythia 8 [21] generator. It uses the NNPDF2.3 [22] set of parton distribution functions (PDF) and a set of tuned parameters called the A14 tune [23]. The $t\bar{t}$, single-top (t- and Wt-channels) and W+jets events were produced at

[1] ATLAS uses a right-handed coordinate system with its origin at the nominal interaction point (IP) in the centre of the detector and the z-axis along the beam line. The x-axis points from the IP to the centre of the LHC ring, and the y-axis points upwards. Cylindrical coordinates (r, ϕ) are used in the transverse plane, ϕ being the azimuthal angle around the beam line. Transverse momentum and energy are defined as $p_{\mathrm{T}} = p \sin\theta$ and $E_{\mathrm{T}} = E \sin\theta$, respectively. The pseudorapidity is defined in terms of the polar angle θ as $\eta = -\ln\tan(\theta/2)$. The angular separation between two objects in η–ϕ space is defined as $\Delta R = \sqrt{(\Delta\eta)^2 + (\Delta\phi)^2}$.

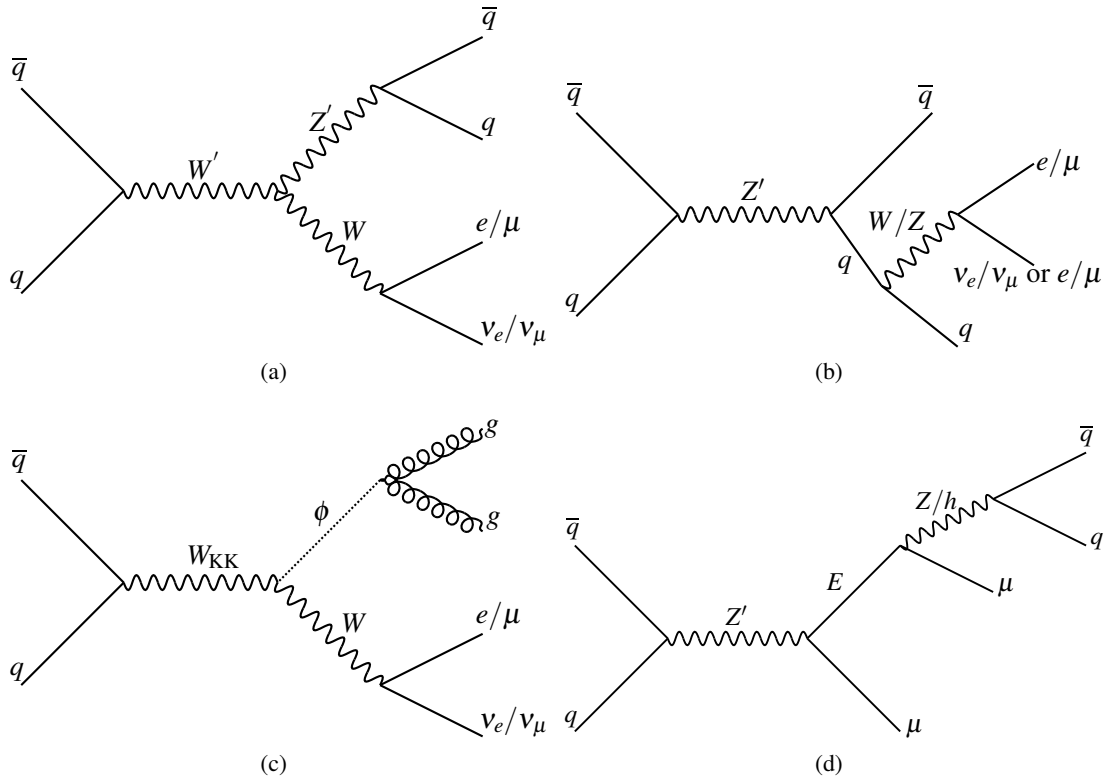

Figure 1: Representative Feynman diagrams for the models considered in this analysis: (a) $W' \to Z' W$ production in the SSM, (b) the simplified DM model, (c) the radion model, (d) the composite-lepton model. The text provides more detailed descriptions.

next-to-leading order in QCD using the POWHEG BOX v2 [24–27] generator interfaced with PYTHIA 8. This simulation uses the CT10NLO PDF set [28] and the AZNLO tune [29].

For the model-dependent searches, MC simulations are also used to predict the expected signal shapes for the BSM models mentioned earlier: (1) $W' \to WZ'$ in the Sequential Standard Model (SSM), (2) a simplified dark-matter (DM) model with an axial-vector mediator Z', (3) a Kaluza–Klein (KK) gauge boson model with a SM W boson and a radion that decays into two gluons, (4) a model with composite $\mathrm{SU(2)_L}$ fermion doublets that breaks lepton-flavour universality ('composite lepton'). Representative Feynman diagrams for these models are shown in Figure 1.

Simulations for the SSM [11] were performed at leading order in QCD using PYTHIA 8 with the CT10NLO PDF set. Event-level simulations for all other BSM models were performed with MADGRAPH5_AMC@NLO [30] at leading order in QCD. The model assumes the heavy Z' boson decays into q and $\bar{q}$, which give rise to two high-energy jets, while the W boson decays leptonically. The $W' \to WZ'$ branching fraction was chosen to be 0.5 and the mass difference between the W' and Z' bosons was set to 250 GeV. The latter setting yields the largest predicted cross-section for the desired final state. This model is also used to estimate systematic uncertainties for the limits when using generic signals approximated by Gaussian functions.

A benchmark simplified DM model [10] includes an axial-vector mediator Z' which decays as $q\bar{q} \to Z' \to q\bar{q}$, and one of the quarks radiates a W or Z boson which then decays via $W/Z \to \ell\nu/\ell\ell$. This model

assumes the leptophobic couplings $g_q = 0.25$, $g_\ell = 0$, and $g_{\mathrm{DM}} = 1$, following the recommendations of the LHC Dark Matter Working Group [10]. Here g_q, g_ℓ and g_{DM} are the couplings of the mediator to quarks, leptons and the DM particle, respectively.

A warped-extra-dimensions model assumes KK excitations of gauge bosons and their decay into a radion and a SM gauge boson, e.g. $q\bar{q} \to W_{\mathrm{KK}} \to \phi W$, followed by $W \to \ell\nu$ and the radion ϕ decaying into a pair of gluons [14, 15]. A mass difference between KK bosons and radions of 250 GeV was chosen for all samples in order to minimise signal peak widths. A larger mass difference leads to the production of higher-p_{T} neutrinos that need to be taken into account in the W_{KK} mass reconstruction.

The composite-lepton model [13] predicts a Z'-like vector boson that decays into a new vector-like composite lepton E along with a SM lepton, $Z' \to E\ell$. The composite lepton E can then decay as $E \to Z/h\,\ell$, with the Z/h boson eventually decaying into two jets. The two leptons produced in this process have sufficient transverse momenta to give higher acceptances in the $m_{jj\ell\ell}$ channel.

The parton showering and hadronisation processes for all the used BSM models were performed using Pythia 8 with the A14 tune. All SM background MC processes were passed through the full ATLAS detector simulation [31] based on Geant4 [32]; samples for the BSM signal processes were simulated using the ATLAS fast simulation framework, ATLFAST-II, which uses parameterisations of electromagnetic and hadronic showers in the calorimeters. Additional simulated pp collisions generated using Pythia 8, with the A3 set of tuned parameters [33] and the NNPDF2.3 PDF set, were overlaid to simulate the effects of pile-up in a manner that matches the multiplicity distribution of additional collisions in the data. Simulated MC events are reconstructed and analysed with the same algorithms as used for data. All simulated events are corrected so that the object identification, reconstruction and trigger efficiencies, energy scales and energy resolution match those determined from data control samples. After these corrections, additional systematic uncertainties are applied to cover differences between the data and MC simulations as described in Section 6.

4 Object definitions and event selection

The analysis presented in this paper is based on data collected with the ATLAS detector during the 2015–2018 data-taking period, referred to as Run 2. The data sample corresponds to an integrated luminosity of 139 fb^{-1} with an uncertainty of 1.7%. The uncertainty was derived from a calibration of the luminosity scale using x–y beam-separation scans, following a methodology similar to that detailed in Ref. [34] and using data from the LUCID-2 detector [35] for the baseline measurement.

Candidate events were accepted by either single-muon or single-electron triggers [19, 36, 37] with various thresholds for the transverse momentum p_{T} of muons or transverse energy E_{T} of electrons, as well as data quality and lepton isolation requirements. The lowest p_{T} (E_{T}) threshold without trigger prescaling is 24 (26) GeV and includes a lepton isolation requirement that is not applied for triggers with higher thresholds. A trigger matching requirement [19] is applied to ensure that the reconstructed lepton lies in the vicinity of the corresponding trigger-level object.

Muons reconstructed from a combination of hits in the ID and MS are required to have $p_{\mathrm{T}} \geq 7$ GeV and $|\eta| \leq 2.5$. They must satisfy 'medium' quality criteria [38]. Identification requirements based on the number of hits in the ID and MS subsystems, as well as the significance of the difference $|q/p_{\mathrm{MS}} - q/p_{\mathrm{ID}}|$, where q is the charge and p_{MS} (p_{ID}) is the momentum as measured in the MS (ID), are applied to the combined tracks. Muon tracks are required to satisfy $|d_0|/\sigma(d_0) \leq 3$ and $|z_0 \sin(\theta)| \leq 0.5$ mm, where

d_0 is the transverse impact parameter relative to the beam line, $\sigma(d_0)$ is its uncertainty, z_0 is the distance along the beam line to the primary vertex from the point where d_0 is measured, and θ is the polar angle of the track. The primary vertex is chosen as the vertex with the highest $\sum p_{\mathrm{T}}^2$, where the sum is over tracks associated with that vertex and having $p_{\mathrm{T}} > 500$ MeV; at least two such tracks are required.

Electrons are identified as energy clusters in the electromagnetic calorimeter [39] matched to tracks in the ID, with requirements of $E_{\mathrm{T}} > 7$ GeV and $|\eta| \leq 2.47$. Candidate electrons must have a track satisfying $|d_0|/\sigma(d_0) \leq 5$ and $|z_0 \sin(\theta)| \leq 0.5$ mm and must meet 'tight' quality criteria [39]. Electrons within the barrel–endcap transition region of the electromagnetic calorimeter, $1.37 \leq |\eta| \leq 1.52$, or which share a track with an identified muon, are discarded.

Leptons are also required to be isolated from other objects in the event, using p_{T}-dependent criteria based on calorimeter and tracking information. The isolation parameters of the FCTight isolation working point [36] were tuned to provide a constant efficiency as a function of transverse momentum, and the highest background rejection below 60 GeV. The lepton isolation and p_{T} requirements allow a consistent definition of lepton candidates when considering data-taking periods in which different trigger configurations were used. Lepton misidentification rates for the chosen isolation requirements are discussed in Refs. [38, 39]. The trigger efficiencies for electrons and muons are above 90% [40, 41].

Jets are reconstructed using the anti-k_t algorithm [42] with a radius parameter of $R = 0.4$, as implemented in the FastJet package [43], using particle-flow objects [44] as inputs. These jets are corrected for contributions arising from additional collisions in the same or neighbouring bunch crossings (pile-up) [45], and calibrated to the particle energy scale (i.e. before interaction with the detector) [46]. Jet candidates must have $p_{\mathrm{T}} \geq 30$ GeV and be within $|\eta| \leq 2.4$. To suppress jets arising from pile-up, a jet-vertex-tagging technique [47, 48] is applied, using the "Tight" working point for central jets with $|\eta| < 2.5$. Jets originating from bottom quarks ('b-jets') are identified using the DL1r algorithm [49, 50] with an offline working point providing 77% b-jet tagging efficiency [51].

An overlap-removal procedure is applied to remove ambiguities which arise when the same object is reconstructed by different algorithms. Candidate jets with fewer than three associated tracks are discarded if they lie within a cone of $\Delta R = 0.2$ around a muon candidate. Jets with any number of associated tracks are discarded if they are within $\Delta R = 0.2$ of an electron. Electron and muon candidates are discarded if they are within a cone of $\Delta R = 0.4$ around the axis of any remaining jets.

Following the lepton and jet selection, a signal region is defined by requiring at least one isolated lepton (e or μ) with $p_{\mathrm{T}}^{\ell} \geq 60$ GeV and at least two jets. The invariant masses are constructed by combining the two jets having the highest p_{T} with one ($m_{jj\ell}$) or two ($m_{jj\ell\ell}$) leptons with the highest p_{T}^{ℓ}. No requirements on the charges of leptons for $m_{jj\ell\ell}$ are applied, as this keeps the selection as model-independent as possible. Invariant masses with at least one b-jet ($m_{jb\ell}$) or two b-jets ($m_{bb\ell}$) are also reconstructed. These invariant masses are sensitive to various BSM scenarios including a few supersymmetric models with R-parity-violating interactions [52, 53].

For all distributions, only events with invariant masses above 0.4 TeV are considered; this minimum value is chosen in order to avoid the low-mass region where the event rate does not decrease monotonically with increasing mass, due to a kinematic bias in jet p_{T} from the minimum-p_{T}^{ℓ} requirement imposed on leptons.

5 Analysis procedure

A new resonant state X with a mass m_X can decay into partons and leptons, either directly or via complex cascade decays. Such decays could lead to an observable excess of events in multi-body invariant masses, such as $m_{jj\ell}$ and $m_{jj\ell\ell}$, near m_X on an otherwise smooth and monotonically decreasing background distribution. This analysis presents a search for such an excess in the mass range above 0.4 TeV for $m_{jj\ell}$, $m_{jj\ell\ell}$, $m_{jb\ell}$ and $m_{bb\ell}$. These signal regions are not orthogonal, with $m_{jj\ell}$ being the most inclusive region, and all other regions being subsets.

The bin widths of the multi-body distributions are chosen to be larger than the resolution for the four-body mass $m_{jj\ell\ell}$, which is fully dominated by the two-jet mass resolution at a given mass. The bin widths are increased from 19 GeV to 148 GeV over the range of 0.4–8 TeV to reflect the changes in the mass resolution. The following fit function is used to model the shape of the estimated background [2, 3, 7, 54]:

$$f(x) = p_1(1-x)^{p_2}x^{p_3+p_4\ln x+p_5\ln^2 x}, \tag{1}$$

where $x \equiv m/\sqrt{s}$ and the p_i ($i = 1, \cdots 5$) are five free parameters. In the following, this function is referred to as a $5p$ function.

According to MC simulations, about 90% of events contributing to $m_{jj\ell}$ originate from the multi-jet background where a jet is misidentified as an electron. The study of such events is limited by the available MC statistics. To investigate the ability of Eq. (1) to accurately describe the background in the signal region, a likelihood fit is performed on a background-enhanced sample obtained from a 'loose electron' control region (LE-CR) defined in data. This control region is dominated by multi-jet events where jets are misidentified as electrons. The LE-CR is populated by selecting events that contain at least two jets and one electron, where the electron satisfies only a set of loose identification criteria and not the more stringent identification criteria that events must satisfy to enter the signal region, thus ensuring orthogonality. The main purpose of this control region is to verify that the data do not show structures that could be interpreted as signals when using the analytic fits. The number of events in the LE-CR is a factor of 10 smaller in the $m_{jj\ell}$ channel than in the signal region, and a factor of 40 smaller in the $m_{jj\ell\ell}$ channel. The $5p$ fit describes the LE-CR well, without structures in the pulls of the fit that could be interpreted as signals.

Due to the over-representation of QCD multi-jet events in the LE-CR, W+jets, $t\bar{t}$ and single-top MC events were added to the LE-CR using the predicted cross-sections. The normalisations of the simulated distributions were set to the expected rate in each signal region to create a hybrid control region (MC+LE-CR). The combined contribution from W boson and top quark processes in the MC simulations varies from 10% to 95% as a function of invariant mass and the b-jet selection. The fit hypothesis of Eq. (1) was validated again for all channels on this MC+LE-CR, and was found to provide a good description for invariant masses above 0.4 TeV, giving $\chi^2/\text{ndf} \simeq 1.37, 0.95, 1.43, 1.28$ for the $m_{jj\ell}$, $m_{jj\ell\ell}$, $m_{jb\ell}$ and $m_{bb\ell}$ distributions respectively, where ndf is the number of degrees of freedom. The distributions of the fit residuals are also consistent with normal distributions with means of zero. The fit parameters are strongly constrained by the low-mass region, below 1 TeV, which has the most events. Functions with the same form as Eq. (1) but with fewer than five parameters fail to describe $m_{jj\ell}$ adequately in the LE-CR and MC+LE-CR regions.

An alternative five-parameter function for the description of the background was investigated. This alternative function, proposed in Ref. [7], differs from Eq. (1) by replacing $p_5\ln^2 x$ with $p_5/\sqrt{x}$. Similarly to the nominal function, applying the alternative function to the LE-CR and MC+LE-CR regions leads to residuals distributed according to a normal distribution with a mean consistent with zero. Differences

between fits of the $m_{jj\ell}$ and $m_{jj\ell\ell}$ distributions with the nominal and alternative functions were statistically insignificant. As the two functions were statistically equivalent when applied to the MC+LE-CR, Eq. (1) was chosen as the nominal function in order to remain consistent with Ref. [7].

To investigate potential biases in the description of the MC+LE-CR by Eq. (1), 'signal-injection' and 'spurious-signal' tests are performed. For the signal-injection test, signal events modelled according to Gaussian distributions are added to the expected background distribution to assess whether or not the correct numbers of events can be extracted using signal-plus-background fits with unconstrained fit parameters, assuming the known Gaussian signal shape. Such tests define signal-injection efficiency correction factors to be applied to the limits. The signal-injection tests are performed for the $m_{jj\ell}$, $m_{jj\ell\ell}$, $m_{jb\ell}$ and $m_{bb\ell}$ distributions, assuming injected signals with various widths from 3% to 15% of the mean mass. The correction factors range from 0.96 to 1.0.

For the spurious-signal test, signal-plus-background fits are run on the background-only spectra of the control region for different signal masses, and the extracted signal yield is taken as an estimate of a potentially false signal. The extracted signal yield in the spurious-signal tests is less than 50% of the statistical uncertainty in each mass bin. This event rate for the signal region is considered as a source of systematic uncertainty in the estimation of cross-section limits (discussed in Section 6).

Based on the studies of the control regions, the background-only hypothesis for the signal region is constructed using Eq. (1), over the mass range starting from 0.4 TeV.

To determine whether the data deviate significantly from the background-only hypothesis, the BumpHunter (BH) algorithm [55] is used. This test calculates the significance of any excess found in mass intervals at all possible locations in the binned invariant mass. The width of the search window varies from a minimum of two bins to half of the full width of the invariant mass distribution. For each of the invariant mass intervals, a local p-value is calculated from a hypothesis-test statistic. The look-elsewhere effect [56] is taken into account by combining the separate hypothesis tests to form a new hypothesis test, and calculating the minimum p-value amongst all tests. A global p-value is then calculated and transformed into a significance by assuming that bin-by-bin fluctuations of the data follow a Poisson distribution. Pseudo-experiments are then used to determine the most significant local excess and, finally, a global significance is calculated. Signal-injection tests show a lower signal-extraction efficiency for wide signals than for narrow signals.

If no statistically significant deviations are observed according to the BH test, upper limits are set at the 95% confidence level (CL) on the production cross-section times branching ratio using the Bayesian method [57] for generic resonances, as well as for the benchmark BSM models discussed in Section 3. Systematic uncertainties are included as nuisance parameters, assuming Gaussian priors. A constant prior is used for the signal normalisation. The 0.95 quantile in the signal contribution is calculated; this is taken as the upper limit on the number of possible signal events in the data, for each resonance mass and width hypothesis. This value, divided by the integrated luminosity, provides a measure of the upper limit on the cross-section times acceptance times efficiency times branching ratio for a resonance with that mass and width. This method is also used to determine the expected limits, along with the corresponding one-standard-deviation (1σ) and two-standard-deviation (2σ) uncertainty bands, using 100 pseudo-experiments.

For the BSM models, the limits calculated using the reconstructed events are corrected for the acceptance and efficiency as a function of the mass. The acceptance is constrained by the p_{T} and η requirements placed on the leptons and jets, and by the minimum dijet invariant mass used in this analysis. The acceptance is typically 50% for the lowest mass point, and increases to 60%–90% for the highest mass, depending on the model. The efficiency correction accounts for various instrumental effects, such as the trigger, lepton

identification, and lepton reconstruction inefficiencies. A typical efficiency, averaged over the two lepton flavours, is 65%–75%, depending on the particle mass and the type of BSM model.

6 Systematic uncertainties

A number of experimental systematic uncertainties are considered for the limit calculations. They are divided into signal-shape-changing uncertainties that affect the limit calculations, uncertainties in the background shape, and uncertainties in efficiencies (and acceptances) that affect the overall normalisation of the final limits for the BSM benchmark models. The first two categories of uncertainties are common to the limit calculations for Gaussian signals and BSM models. Systematic uncertainties affecting the shapes of invariant mass distributions are estimated from the BSM MC event samples. They are included as nuisance parameters in the calculation of the Bayesian limits. The uncertainty of 1.7% in the integrated luminosity is used for all limits.

The effects of jet energy scale (JES) and jet energy resolution (JER) uncertainties [46] are estimated using signal model MC events. The combined effect of all the systematic uncertainties is to raise the cross-section upper limits relative to the limits without uncertainties. This effect has a typical size comparable to the width of the 1σ statistical uncertainty band around the expected limits. Uncertainties related to b-jet tagging are included in the $m_{jb\ell}$ and $m_{bb\ell}$ invariant masses. The JES uncertainty accounts for more than 50% of the total systematic uncertainty, while the JER uncertainty makes the second-largest contribution. The effect of lepton energy scale and resolution uncertainties is found to be negligible. The effects of lepton trigger, identification and reconstruction uncertainties, contributing to differences between data and MC events, are taken into account by assigning a combined uncertainty of 1%.

For the generic Gaussian signals, JES and JER systematic uncertainties from the $W' \to WZ' \to \ell\nu\, q\bar{q}$ MC events are used, parameterised as a function of mass to generate uncertainties for mass values that were not used in generating the $W' \to WZ'$ samples. As a cross-check, other models predicting different signal widths are also used, but no significant differences are observed.

The uncertainties arising from imperfect knowledge of the background shapes are investigated by using the alternative background fit and the spurious-signal test (discussed previously) using the nominal $5p$ fit to the data. The uncertainty due to the choice of background function is estimated by performing the background fit with the alternative fit function. The difference between the results of this fit and the nominal one, averaged across a set of pseudo-data, is considered as a systematic uncertainty. Both uncertainties are found to have a negligible effect on the limits.

Uncertainties in the efficiency and acceptance correction factors related to JES, JER, b-jet and lepton identification (and reconstruction) are found to be smaller than 1%. An additional uncertainty in the limits is associated with the PDF choice for the acceptance calculation [58]. This is accounted for by assigning a 1% PDF uncertainty to the calculated limits.

7 Results

Figures 2, 3 and 4 show the invariant mass distributions discussed above, together with the results of the likelihood fits using the $5p$ function from Eq. (1). The quality of the fit in terms of the χ^2/ndf is indicated. In order to establish the presence or absence of a signal in the $m_{jj\ell}$ distribution, the BH algorithm is used.

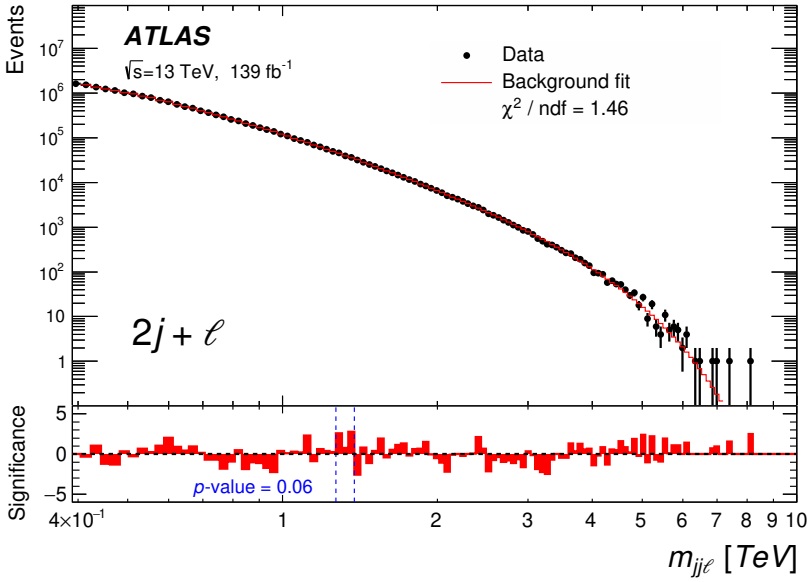

Figure 2: Invariant $2j + \ell$ mass distribution for $m_{jj\ell} > 0.4$ TeV together with the fit with the $5p$ background function. The lower panel shows the bin-by-bin significances of deviations from the background hypothesis. The largest deviation reported by the BumpHunter algorithm is shown by the vertical dashed lines. The global p-value of this deviation in the range 1.27–1.38 TeV is indicated.

It is also used to calculate local and global significances of the largest deviation from the background hypothesis.

Figure 2 shows the invariant mass distribution $m_{jj\ell}$ obtained from the selected $2j + \ell$ events. The data are described by the $5p$ fit function, with $\chi^2 = 149$ and ndf = 102. The lower panel shows the significances [59] of deviations from the background hypothesis, which can be approximated by $(d_i - f_i)/\delta_i$, where d_i is the number of events in the bin i, f_i is the fit value, and δ_i is an uncertainty. This uncertainty includes the statistical and systematic uncertainties of the fit result f_i.

The largest deviation of the $m_{jj\ell}$ data from the background-only hypothesis reported by the BH is near 1.3 TeV, with a local p-value of 2×10^{-5}, corresponding to a significance of 3.5 standard deviations. Accounting for the look-elsewhere effect for the $m_{jj\ell}$ distribution, the global p-value for the largest deviation using the nominal fit is 0.06, leading to a global significance of 1.5σ. When using the alternative background fit, this deviation has a lower local significance of 2.8σ. This deviation from the background hypothesis is thus consistent with a statistical fluctuation.

The deviation near 1.3 TeV is equally present in the electron and muon channels, but its statistical significance is smaller than for the combined channel. For the separate channels, the BH reports that the largest deviations are in the region near 5 TeV. The global p-values for the deviations near 5 TeV are 0.13 (for muons) and 0.38 (for electrons). Thus, such deviations from the $5p$ background are also consistent with statistical fluctuations.

Figure 3 shows the $m_{jj\ell\ell}$ mass distribution for the combined muon and electron channels. The global p-value for the largest deviation, near 4 TeV, is 0.69, indicating no significant deviations from the $5p$ background. The separate muon and electron channels do not show significant deviations.

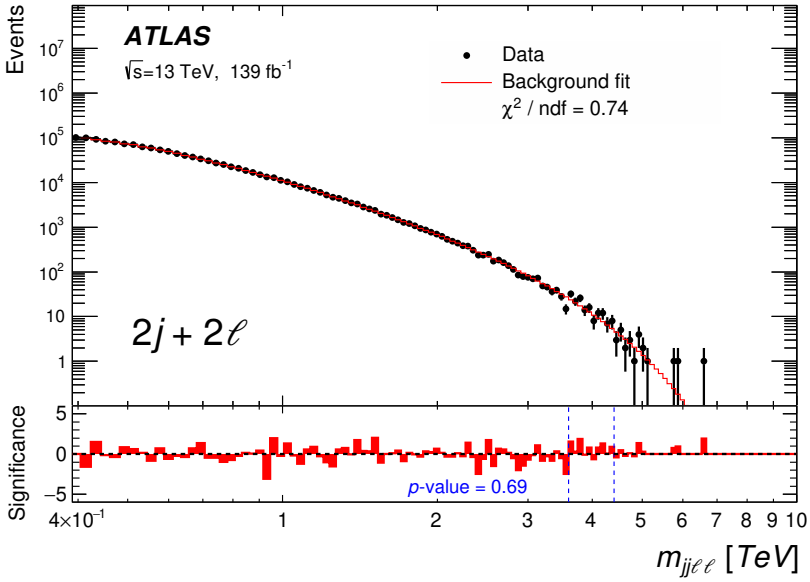

Figure 3: Invariant $2j + 2\ell$ mass distribution for $m_{jj\ell\ell} > 0.4$ TeV together with the fit with the $5p$ background function. The lower panel shows the bin-by-bin significances of deviations from the background hypothesis. The largest deviation reported by the BumpHunter algorithm is shown by the vertical dashed lines. The global p-value of this deviation in the range 3.59–4.41 TeV is indicated.

Figure 4 shows the distributions for three-body masses with one or two b-jets. The global p-values for the largest deviations are larger than 0.6. Thus the distributions do not show significant deviations from the background.

7.1 Model-independent limits

In the absence of any statistically significant deviations from the $5p$ background function, the Bayesian method is used to set 95% CL upper limits on the cross-section for new processes that have a signature of a new particle with decays producing two jets and leptons. The limits are obtained for hypothetical signals with a Gaussian shape.[2]

Figure 5 shows the 95% CL expected and observed limits on the cross-section times acceptance (A), signal efficiency (ϵ) and branching ratio (B) of a BSM particle decaying into two jets and a lepton. The observed limits are shown for different widths, ranging from a narrow width – comparable to the experimental resolution of about 3% – up to 15% of the mean mass. The expected limit and the corresponding $\pm 1\sigma$ and $\pm 2\sigma$ bands are shown for narrow width ($\sigma_X/m_X = 0$) resonances. As expected, the limits are weaker for broader resonances that span more $m_{jj\ell}$ bins. Signals making Gaussian contributions to the $m_{jj\ell}$ distribution are excluded by the obtained limits as a function of the mean mass. The expected limit and the corresponding $\pm 1\sigma$ and $\pm 2\sigma$ bands are shown for the narrowest Gaussian width. The observed exclusion limits range from 20 fb to 0.1 fb in the mass range 0.5–8 TeV.

[2] Using the Gaussian limits requires some care in treating the realistic shapes from specific models. For example, the appendix of Ref. [60] gives a recipe for how the Gaussian limits should be used for dijet studies.

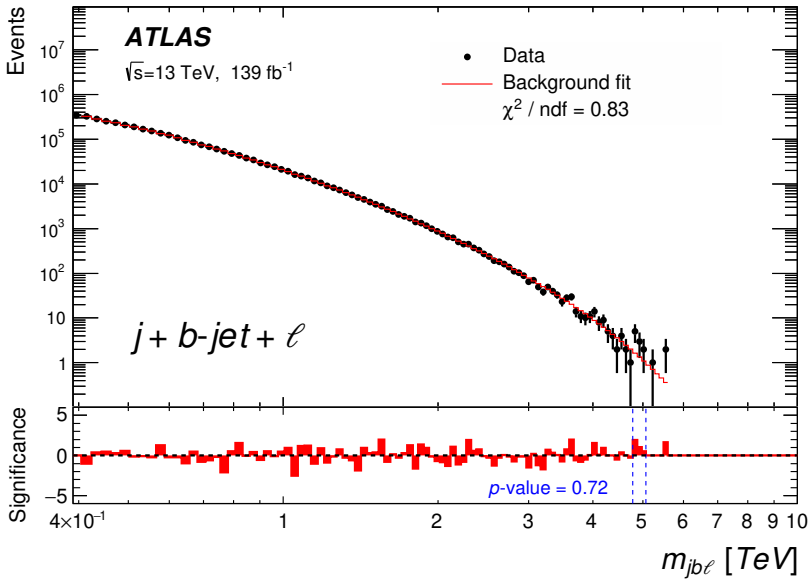

(a) $m_{jb\ell}$ invariant mass

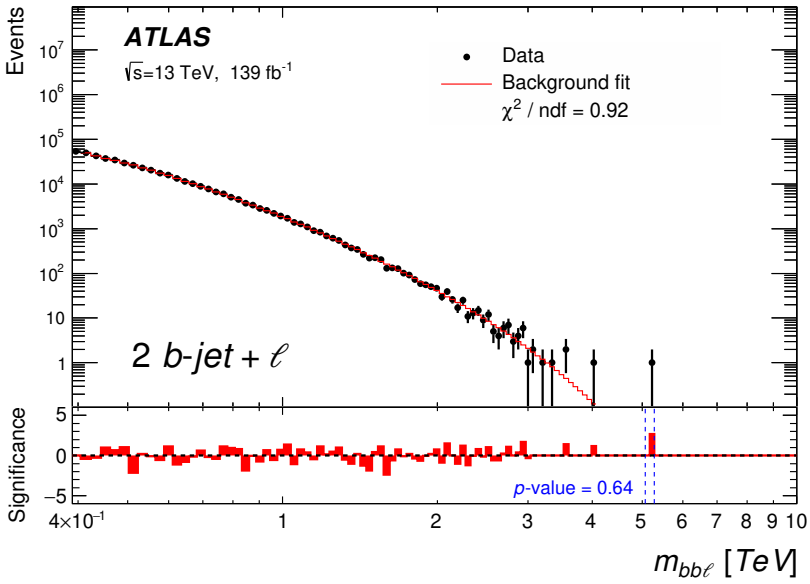

(b) $m_{bb\ell}$ invariant mass

Figure 4: Invariant mass distributions (a) $m_{jb\ell}$ and (b) $m_{bb\ell}$ with the $5p$ background fits. The lower panels show the bin-by-bin significances of deviations from the background hypothesis. The largest deviations reported by the BumpHunter algorithm are indicated by the vertical dashed lines. The global p-values of these deviations in the range 4.78–5.07 TeV (for $m_{jb\ell}$) and 5.07–5.27 TeV (for $m_{bb\ell}$) are indicated.

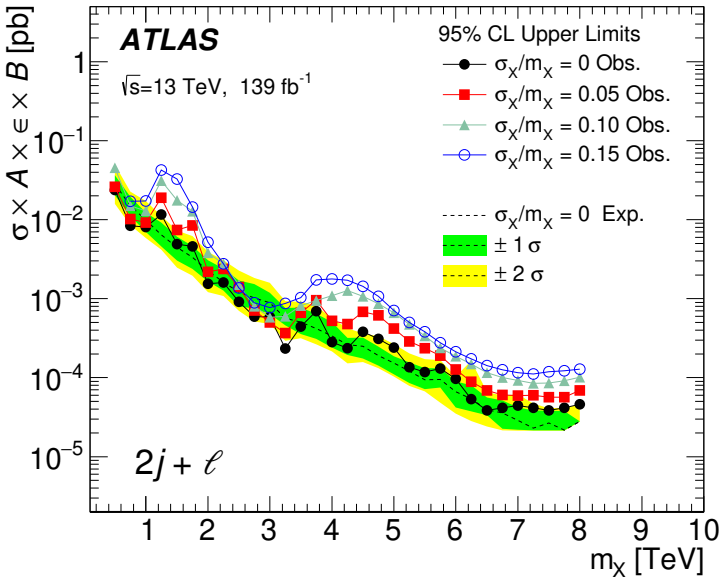

Figure 5: The 95% CL observed upper limits, in the $m_{jj\ell}$ channel, on the cross-section times acceptance (A), efficiency (ϵ) and branching ratio (B) for a Gaussian signal with various signal widths. The expected limit and the corresponding $\pm 1\sigma$ and $\pm 2\sigma$ bands are shown for $\sigma_X/m_X = 0$ signals. The limit for a width of 15% is shown starting from 0.75 TeV in order to avoid the region close to the minimum value of the $m_{jj\ell}$ distribution.

Figure 6 shows the observed limits for four-body invariant masses, $m_{jj\ell\ell}$. The limits are obtained for Gaussian signals with different widths, from a narrow width – compatible with the experimental resolution – up to 15% of the mean mass. Figure 7(a) shows similar Gaussian limits for the $m_{jb\ell}$ distribution. Figure 7(b) shows the observed limits for the $m_{bb\ell}$ invariant mass. The obtained limits range from about 10 fb to 0.1 fb for resonance masses between 0.5 TeV and 4–5 TeV.

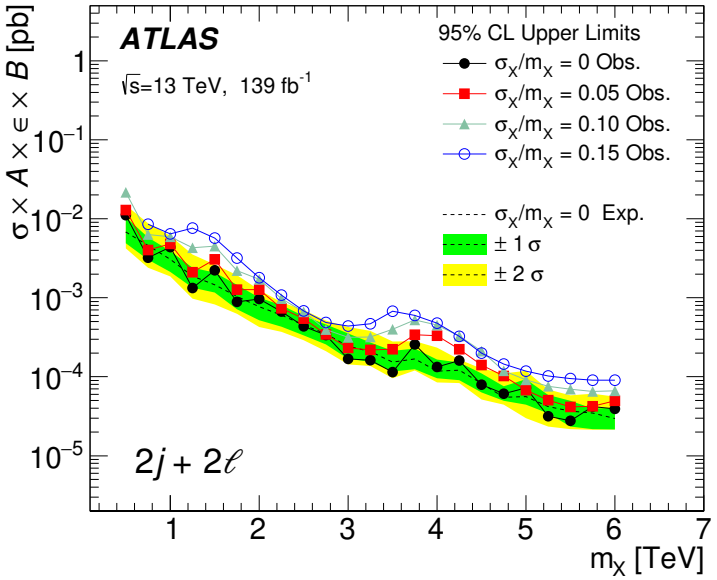

Figure 6: The 95% CL observed upper limits, in the $m_{jj\ell\ell}$ channel, on the cross-section times acceptance (A), efficiency (ϵ) and branching ratio (B) for a Gaussian signal with various signal widths. The expected limit and the corresponding $\pm 1\sigma$ and $\pm 2\sigma$ bands are shown for $\sigma_X/m_X = 0$ signals. The limit for a width of 15% is shown starting from 0.75 TeV in order to avoid the region close to the minimum value of the $m_{jj\ell\ell}$ distribution.

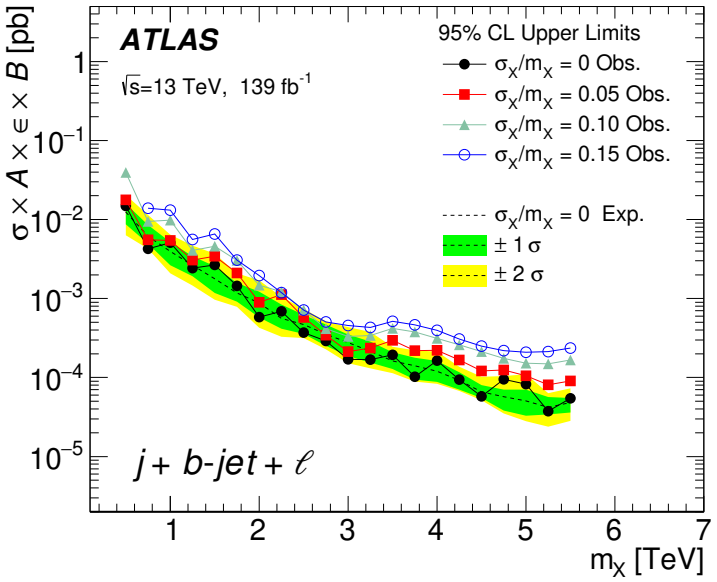

(a) Limits for $m_{jb\ell}$

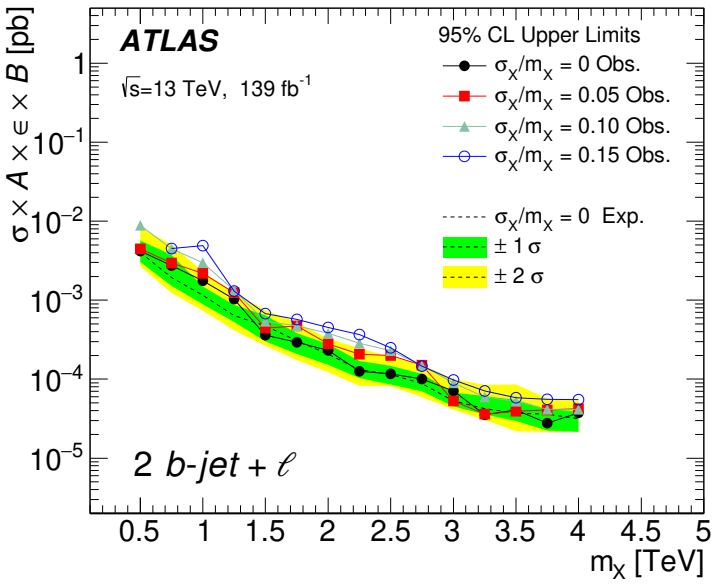

(b) Limits for $m_{bb\ell}$

Figure 7: The 95% CL observed upper limits, in the $m_{jb\ell}$ and $m_{bb\ell}$ channels, on the cross-section times acceptance (A), efficiency (ϵ) and branching ratio (B) for a Gaussian signal with various signal widths. The expected limits and the corresponding $\pm 1\sigma$ and $\pm 2\sigma$ bands are shown for $\sigma_X/m_X = 0$ signals. The limits for a width of 15% are shown starting from 0.75 TeV in order to avoid the region close to the minimum value of the invariant mass distributions.

7.2 Limits on BSM models

To calculate the exclusion limits for the benchmark models, the exact shapes of the $m_{jj\ell}$ and $m_{jj\ell\ell}$ distributions of the signal MC events after simulation and reconstruction are used. The Bayesian limits are calculated using the $m_{jj\ell}$ and $m_{jj\ell\ell}$ distributions with the background description discussed earlier, and then the acceptance and efficiency corrections are applied. The limits on the composite-lepton model are calculated using $m_{jj\ell\ell}$ in the muon channel for two masses, 250 GeV and 500 GeV, of a composite lepton E. The muon channel was chosen for this model as the Z' preferentially couples to muons over electrons. The calculated limits include the systematic uncertainties discussed in Section 6.

Figures 8 and 9 show the observed (filled circles) and expected (dotted line with uncertainty bands) 95% CL upper limits on the cross-section times branching ratios. These results exclude contributions from the $W' \to WZ'$ process in the SSM for masses of the W' boson (decaying into jet pairs) below 2.5 TeV and a mass difference of 250 GeV between the W' and Z' bosons, which maximises the cross-section for this process. This is consistent with the previous result for the same model using dijet events, where a Z' boson (decaying into jet pairs) with a mass below 2 TeV was excluded [7]. For the radion model, in which the mass-splitting between a radion ϕ and W_{KK} is small (250 GeV), the data exclude ϕ with a mass below 1 TeV, as shown in Figure 8(b). For the studied mass range, the current analysis cannot exclude the DM model with a Z' axial-vector mediator, as seen in Figure 8(c). Figure 9 shows the limits for the composite-lepton model with a Z' boson. The data exclude a Z' boson with a mass below 1.3 TeV for a composite lepton mass of 500 GeV.

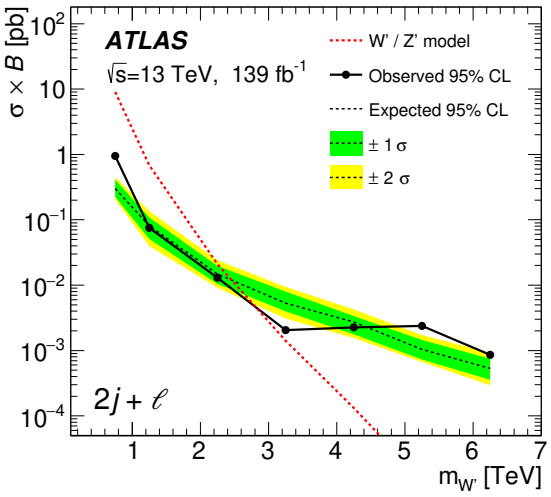

(a) SSM model

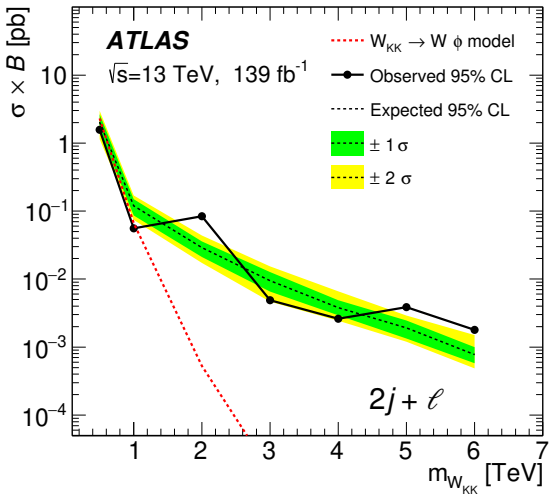

(b) $W_{\mathrm{KK}} + \phi$ model

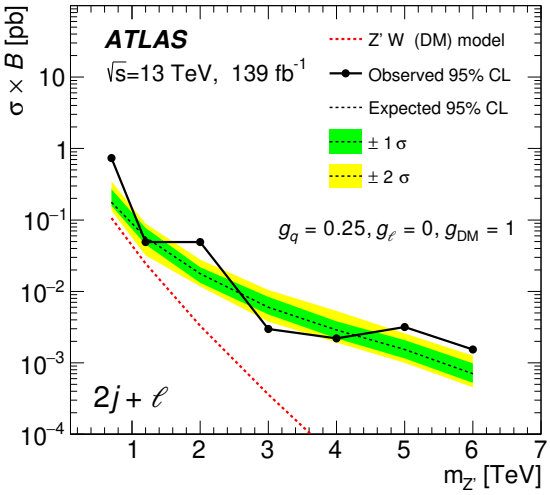

(c) $Z'W$ (DM) model

Figure 8: Observed (filled circles) and expected (dotted line with uncertainty bands) 95% CL upper limits on the cross-section (σ) times branching ratio (B) for (a) the SSM W' boson, (b) the $W_{\mathrm{KK}} + \phi$ radion model with $m_{W_{\mathrm{KK}}} - m_{\phi} = 250$ GeV, and (c) the $Z'W$ simplified DM model. The presented limits were obtained using the $m_{jj\ell}$ ($\ell = \mu, e$) distribution in events with at least one isolated lepton with $p_{\mathrm{T}}^{\ell} > 60$ GeV. Branching ratios of 100% to the final states of interest were assumed in the signal generation and computation of theory cross-sections. The black lines shown for the observed limits are provided to guide the eye.

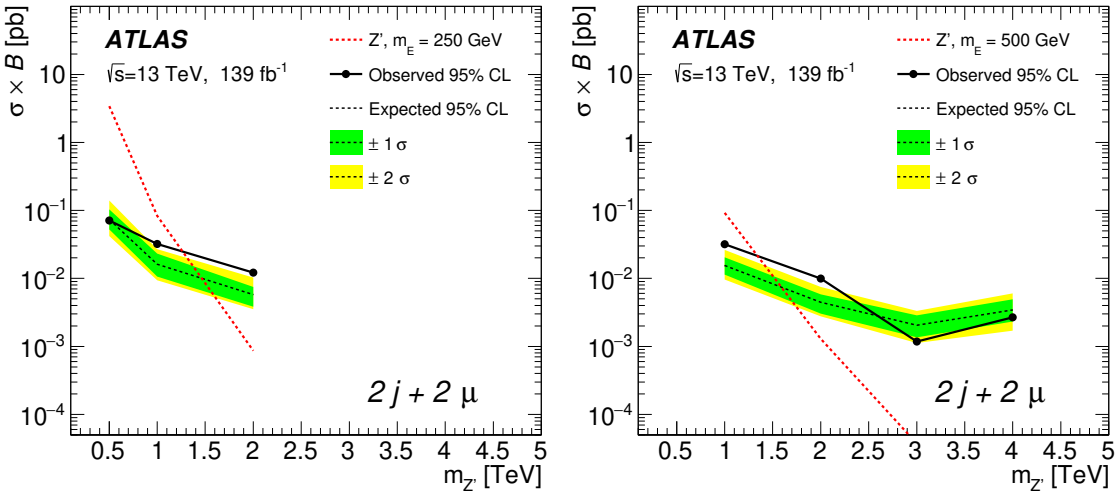

(a) Composite-lepton model with $m_E = 250$ GeV

(b) Composite-lepton model with $m_E = 500$ GeV

Figure 9: Observed (filled circles) and expected (dotted line with uncertainty bands) 95% CL upper limits on the cross-section (σ) times branching ratio (B) for $Z' \to E\mu$ where the composite lepton E has a mass of (a) 250 GeV or (b) 500 GeV. The presented limits were obtained using the $m_{jj\ell\ell}$ ($\ell = \mu$) distribution in events with at least one isolated muon with $p_{\mathrm{T}}^{\ell} > 60$ GeV. Branching ratios of 100% to the final states of interest were assumed in the signal generation and computation of theory cross-sections. The black lines shown for the observed limits are provided to guide the eye.

8 Conclusion

A model-independent search for new resonances in invariant masses constructed from jets and leptons with $p_{\mathrm{T}}^{\ell} > 60$ GeV using an integrated luminosity of 139 fb^{-1} of proton–proton collisions with a centre-of-mass energy of $\sqrt{s} = 13$ TeV recorded by the ATLAS detector at the LHC is presented. Several three- and four-body invariant masses were studied: $m_{jj\ell}$, $m_{jj\ell\ell}$, $m_{jb\ell}$ and $m_{bb\ell}$ in the mass range from 0.4 to 8 TeV. For the first time, searches in these invariant masses are performed with a data-driven technique, assuming a smoothly falling background described by a fit function, without relying on statistically limited MC predictions.

The multi-body invariant masses do not exhibit significant excesses above a data-derived estimate of the smoothly falling background. The most significant deviation from the data-derived estimate of the SM background in the combined electron and muon channel is observed around $m_{jj\ell} = 1.3$ TeV. This excess has a local statistical significance of 3.5 standard deviations. After accounting for the look-elsewhere effect, this deviation corresponds to a global statistical significance of 1.5σ. A check with an alternative description leads to a lower local significance of 2.8σ. Other multi-body invariant-mass combinations show smaller local deviations. Thus the data are consistent with the background-only hypothesis.

In the absence of signals indicating the presence of new phenomena, this analysis sets 95% CL upper limits on the cross-section times acceptance, efficiency and branching fraction for new processes that can produce a Gaussian contribution to the invariant mass distributions of jets and leptons. The limits are calculated for a Gaussian width ranging from that determined by the detector resolution up to 15% of the resonance mass.

These results exclude generic BSM models predicting resonances that decay to produce jets and leptons with cross-sections larger than the limits reported in this paper. This study extends the search range by 2 TeV beyond that of previous searches which did not include leptons in the invariant masses.

Model-dependent limits are also set on a variety of BSM models, without the use of additional selection criteria tailored to the specific final states investigated. These results exclude contributions from the $W' \to WZ'$ process in the SSM for masses of a W' boson below 2.5 TeV, assuming the mass difference between the W' and Z' bosons is 250 GeV to maximise the cross-section for this process. For the radion model, in which the mass-splitting between a radion ϕ and W_{KK} is small (250 GeV), the data exclude ϕ at masses below 1 TeV. For the composite-lepton model with a Z' boson, the data exclude a Z' boson with a mass below 1.3 TeV for a composite lepton mass of 500 GeV.

References

[1] ATLAS Collaboration, *Search for new resonances in mass distributions of jet pairs using 139 fb^{-1} of pp collisions at $\sqrt{s}$ = 13 TeV with the ATLAS detector*, JHEP **03** (2020) 145, arXiv: 1910.08447 [hep-ex].

[2] ATLAS Collaboration, *Search for low-mass resonances decaying into two jets and produced in association with a photon using pp collisions at $\sqrt{s}$ = 13 TeV with the ATLAS detector*, Phys. Lett. B **795** (2019) 56, arXiv: 1901.10917 [hep-ex].

[3] ATLAS Collaboration, *Search for Low-Mass Dijet Resonances Using Trigger-Level Jets with the ATLAS Detector in pp Collisions at $\sqrt{s}$ = 13 TeV*, Phys. Rev. Lett. **121** (2018) 081801, arXiv: 1804.03496 [hep-ex].

[4] CMS Collaboration, *Search for high mass dijet resonances with a new background prediction method in proton-proton collisions at $\sqrt{s}$ = 13 TeV*, JHEP **05** (2020) 033, arXiv: 1911.03947 [hep-ex].

[5] CMS Collaboration, *Search for narrow resonances in the b-tagged dijet mass spectrum in proton-proton collisions at $\sqrt{s}$ = 13 TeV*, (2022), arXiv: 2205.01835 [hep-ex].

[6] CMS Collaboration, *Search for dijet resonances using events with three jets in proton-proton collisions at $\sqrt{s}$=13 TeV*, Phys. Lett. B **805** (2020) 135448, arXiv: 1911.03761 [hep-ex].

[7] ATLAS Collaboration, *Search for dijet resonances in events with an isolated charged lepton using $\sqrt{s}$ = 13 TeV proton-proton collision data collected by the ATLAS detector*, JHEP **06** (2020) 151, arXiv: 2002.11325 [hep-ex].

[8] *A search for new resonances in multiple final states with a high transverse momentum Z boson in $\sqrt{s}$ = 13 TeV pp collisions with the ATLAS detector*, (2022), arXiv: 2209.15345 [hep-ex].

[9] S. Chekanov, S. Darmora, W. Islam, C. E. M. Wagner and J. Zhang, *Model-Independent Searches for New Physics in Multi-Body Invariant Masses*, Universe **7** (2021) 333, arXiv: 2103.10217 [hep-ph].

[10] D. Abercrombie et al., *Dark Matter benchmark models for early LHC Run-2 Searches: Report of the ATLAS/CMS Dark Matter Forum*, Phys. Dark Univ. **27** (2020) 100371, arXiv: 1507.00966 [hep-ex].

[11] G. Altarelli, B. Mele and M. Ruiz-Altaba, *Searching for new heavy vector bosons in $p\bar{p}$ colliders*, Z. Phys. C **45** (1989) 109; *Erratum*, Z. Phys. C **47** (1990) 676.

[12] A. Roitgrund and G. Eilam, *Search for like-sign dileptons plus two jets signal in the framework of the manifest left-right symmetric model*, JHEP **01** (2021) 031, [Erratum: JHEP 03, 029 (2021)], arXiv: 1704.07772 [hep-ph].

[13] M. Chala and M. Spannowsky, *Behavior of composite resonances breaking lepton flavor universality*, Phys. Rev. D **98** (2018) 035010, arXiv: 1803.02364 [hep-ph].

[14] K. Agashe et al., *Dedicated strategies for triboson signals from cascade decays of vector resonances*, Phys. Rev. D **99** (2019) 075016, arXiv: 1711.09920 [hep-ph].

[15] K. S. Agashe et al., *LHC signals from cascade decays of warped vector resonances*, JHEP **05** (2017) 078, arXiv: 1612.00047 [hep-ph].

[16] ATLAS Collaboration, *The ATLAS Experiment at the CERN Large Hadron Collider*, JINST **3** (2008) S08003.

[17] ATLAS Collaboration, *ATLAS Insertable B-Layer Technical Design Report*, ATLAS-TDR-19; CERN-LHCC-2010-013, 2010, URL: https://cds.cern.ch/record/1291633, Addendum: ATLAS-TDR-19-ADD-1; CERN-LHCC-2012-009, 2012, URL: https://cds.cern.ch/record/1451888.

[18] B. Abbott et al., *Production and integration of the ATLAS Insertable B-Layer*, JINST **13** (2018) T05008, arXiv: 1803.00844 [physics.ins-det].

[19] ATLAS Collaboration, *Performance of the ATLAS trigger system in 2015*, Eur. Phys. J. C **77** (2017) 317, arXiv: 1611.09661 [hep-ex].

[20] ATLAS Collaboration, *The ATLAS Collaboration Software and Firmware*, ATL-SOFT-PUB-2021-001, 2021, URL: https://cds.cern.ch/record/2767187.

[21] T. Sjostrand, S. Mrenna and P. Z. Skands, *A Brief Introduction to PYTHIA 8.1*, Comput. Phys. Commun. **178** (2008) 852, arXiv: 0710.3820 [hep-ph].

[22] R. D. Ball et al., *Parton distributions with LHC data*, Nucl. Phys. B **867** (2013) 244, arXiv: 1207.1303 [hep-ph].

[23] ATLAS Collaboration, *ATLAS Pythia 8 tunes to* 7 *TeV data*, ATL-PHYS-PUB-2014-021, 2014, URL: https://cds.cern.ch/record/1966419.

[24] P. Nason, *A new method for combining NLO QCD with shower Monte Carlo algorithms*, JHEP **11** (2004) 040, arXiv: hep-ph/0409146.

[25] S. Frixione, P. Nason and C. Oleari, *Matching NLO QCD computations with parton shower simulations: the POWHEG method*, JHEP **11** (2007) 070, arXiv: 0709.2092 [hep-ph].

[26] S. Alioli, P. Nason, C. Oleari and E. Re, *A general framework for implementing NLO calculations in shower Monte Carlo programs: the POWHEG BOX*, JHEP **06** (2010) 043, arXiv: 1002.2581 [hep-ph].

[27] S. Frixione, P. Nason and G. Ridolfi, *A positive-weight next-to-leading-order Monte Carlo for heavy flavour hadroproduction*, JHEP **09** (2007) 126, arXiv: 0707.3088 [hep-ph].

[28] H.-L. Lai et al., *New parton distributions for collider physics*, Phys. Rev. D **82** (2010) 074024, arXiv: 1007.2241 [hep-ph].

[29] ATLAS Collaboration, *Measurement of the Z/γ^* boson transverse momentum distribution in pp collisions at $\sqrt{s} = 7$ TeV with the ATLAS detector*, JHEP **09** (2014) 145, arXiv: 1406.3660 [hep-ex].

[30] J. Alwall et al., *The automated computation of tree-level and next-to-leading order differential cross sections, and their matching to parton shower simulations*, JHEP **07** (2014) 079, arXiv: 1405.0301 [hep-ph].

[31] ATLAS Collaboration, *The ATLAS Simulation Infrastructure*, Eur. Phys. J. C **70** (2010) 823, arXiv: 1005.4568 [physics.ins-det].

[32] S. Agostinelli et al., GEANT4 – *a simulation toolkit*, Nucl. Instrum. Meth. A **506** (2003) 250.

[33] ATLAS Collaboration, *The Pythia 8 A3 tune description of ATLAS minimum bias and inelastic measurements incorporating the Donnachie–Landshoff diffractive model*, ATL-PHYS-PUB-2016-017, 2016, URL: https://cds.cern.ch/record/2206965.

[34] ATLAS Collaboration, *Luminosity determination in pp collisions at $\sqrt{s} = 13$ TeV using the ATLAS detector at the LHC*, ATLAS-CONF-2019-021, 2019, URL: https://cds.cern.ch/record/2677054.

[35] G. Avoni et al., *The new LUCID-2 detector for luminosity measurement and monitoring in ATLAS*, JINST **13** (2018) P07017.

[36] ATLAS Collaboration, *Performance of electron and photon triggers in ATLAS during LHC Run 2*, Eur. Phys. J. C **80** (2020) 47, arXiv: 1909.00761 [hep-ex].

[37] ATLAS Collaboration, *Performance of the ATLAS muon triggers in Run 2*, JINST **15** (2020) P09015, arXiv: 2004.13447 [physics.ins-det].

[38] ATLAS Collaboration, *Muon reconstruction performance of the ATLAS detector in proton–proton collision data at $\sqrt{s}$ =13 TeV*, Eur. Phys. J. C **76** (2016) 292, arXiv: 1603.05598 [hep-ex].

[39] ATLAS Collaboration, *Electron and photon performance measurements with the ATLAS detector using the 2015–2017 LHC proton-proton collision data*, JINST **14** (2019) P12006, arXiv: 1908.00005 [hep-ex].

[40] ATLAS Collaboration, *Single electron trigger 2018 performance plots*, tech. rep. ATL-COM-DAQ-2019-049, CERN, 2019, URL: https://cds.cern.ch/record/2668252.

[41] ATLAS Collaboration, *Muon reconstruction and identification efficiency in ATLAS using the full Run 2 pp collision data set at $\sqrt{s} = 13$ TeV*, Eur. Phys. J. C **81** (2021) 578, arXiv: 2012.00578 [hep-ex].

[42] M. Cacciari, G. P. Salam and G. Soyez, *The anti-k_t jet clustering algorithm*, JHEP **04** (2008) 063, arXiv: 0802.1189 [hep-ph].

[43] M. Cacciari, G. P. Salam and G. Soyez, *FastJet user manual*, Eur. Phys. J. C **72** (2012) 1896, arXiv: 1111.6097 [hep-ph].

[44] ATLAS Collaboration, *Jet reconstruction and performance using particle flow with the ATLAS Detector*, Eur. Phys. J. C **77** (2017) 466, arXiv: 1703.10485 [hep-ex].

[45] ATLAS Collaboration, *Tagging and suppression of pileup jets with the ATLAS detector*, ATLAS-CONF-2014-018, 2014, URL: https://cds.cern.ch/record/1700870.

[46] ATLAS Collaboration, *Jet energy scale and resolution measured in proton–proton collisions at $\sqrt{s} = 13$ TeV with the ATLAS detector*, Eur. Phys. J. C **81** (2021) 689, arXiv: 2007.02645 [hep-ex].

[47] ATLAS Collaboration, *Performance of pile-up mitigation techniques for jets in pp collisions at $\sqrt{s} = 8$ TeV using the ATLAS detector*, Eur. Phys. J. C **76** (2016) 581, arXiv: 1510.03823 [hep-ex].

[48] ATLAS Collaboration, *Forward jet vertex tagging using the particle flow algorithm*, ATL-PHYS-PUB-2019-026, 2019, URL: https://cds.cern.ch/record/2683100.

[49] ATLAS Collaboration, *ATLAS b-jet identification performance and efficiency measurement with $t\bar{t}$ events in pp collisions at $\sqrt{s}$ = 13 TeV*, Eur. Phys. J. C **79** (2019) 970, arXiv: 1907.05120 [hep-ex].

[50] ATLAS Collaboration, *Monte Carlo to Monte Carlo scale factors for flavour tagging efficiency calibration*, ATL-PHYS-PUB-2020-009, 2020, URL: https://cds.cern.ch/record/2718610.

[51] ATLAS Collaboration, *Flavour-tagging efficiency corrections for the 2019 ATLAS PFlow jet and VR track jets b-taggers with the full LHC Run II dataset*, Web page, URL: http://atlas.web.cern.ch/Atlas/GROUPS/PHYSICS/PLOTS/FTAG-2021-001.

[52] D. Das, C. Hati, G. Kumar and N. Mahajan, *Scrutinizing R-parity violating interactions in light of $R_{K^{(*)}}$ data*, Phys. Rev. D **96** (2017) 095033, arXiv: 1705.09188 [hep-ph].

[53] K. Earl and T. Grégoire, *Contributions to $b \to s\ell\ell$ anomalies from R-parity violating interactions*, JHEP **08** (2018) 201, arXiv: 1806.01343 [hep-ph].

[54] ATLAS Collaboration, *Search for new phenomena in the dijet mass distribution using pp collision data at $\sqrt{s}$ = 8 TeV with the ATLAS detector*, Phys. Rev. D **91** (2015) 052007, arXiv: 1407.1376 [hep-ex].

[55] G. Choudalakis, *On hypothesis testing, trials factor, hypertests and the BumpHunter*, tech. rep., 2011, arXiv: 1101.0390 [physics.data-an].

[56] E. Gross and O. Vitells, *Trial factors for the look elsewhere effect in high energy physics*, Eur. Phys. J. C **70** (2010) 525, arXiv: 1005.1891 [physics.data-an].

[57] A. Caldwell, D. Kollar and K. Kroninger, *BAT – The Bayesian analysis toolkit*, Comput. Phys. Commun. **180** (2009) 2197, arXiv: 0808.2552 [physics.data-an].

[58] ATLAS Collaboration, *Search for new phenomena in dijet events using 37 fb^{-1} of pp collision data collected at $\sqrt{s}$ =13 TeV with the ATLAS detector*, Phys. Rev. D **96** (2017) 052004, arXiv: 1703.09127 [hep-ex].

[59] G. Choudalakis and D. Casadei, *Plotting the differences between data and expectation*, Eur. Phys. J. Plus **127** (2012) 25, arXiv: 1111.2062 [physics.data-an].

[60] ATLAS Collaboration, *Search for new phenomena in the dijet mass distribution using $p - p$ collision data at $\sqrt{s}$ = 8 TeV with the ATLAS detector*, Phys. Rev. D **91** (2015) 052007, arXiv: 1407.1376 [hep-ex].